Physics in Medicine & Biology

PAPER • OPEN ACCESS

# Fabrication and characterization of a multimodal 3D printed mouse phantom for ionoacoustic quality assurance in image-guided pre-clinical proton radiation research

To cite this article: Julie Lascaud *et al* 2022 *Phys. Med. Biol.* **67** 205001

View the article online for updates and enhancements.

You may also like

- Studies of a prototype linear stationary x-ray source for tomosynthesis imaging
P R Schwoebel, John M Boone and Joe Shao
- Development of an anatomically correct mouse phantom for dosimetry measurement in small animal radiotherapy research
George Soultanidis, Anna Subiel, Isaline Renard et al.
- Imaging performance of LabPET APD-based digital PET scanners for pre-clinical research
Mélanie Bergeron, Jules Cadorette, Marc-André Tétrault et al.

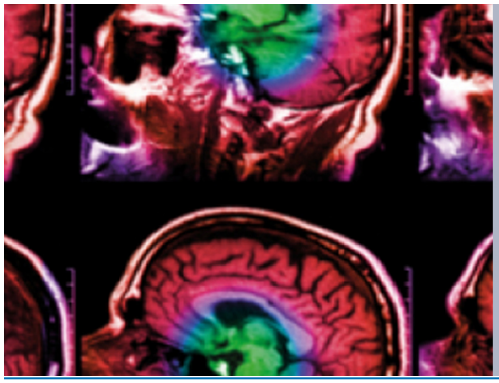

IPEM | IOP
Series in Physics and Engineering in Medicine and Biology

Your publishing choice in medical physics, biomedical engineering and related subjects.

Start exploring the collection–download the first chapter of every title for free.

This content was downloaded from IP address 212.114.229.233 on 28/11/2022 at 07:12

IOP Publishing Phys. Med. Biol. 67 (2022) 205001 https://doi.org/10.1088/1361-6560/ac9031

Physics in Medicine & Biology

IPEM Institute of Physics and Engineering in Medicine

CrossMark

OPEN ACCESS

RECEIVED
20 May 2022

REVISED
13 August 2022

ACCEPTED FOR PUBLICATION
6 September 2022

PUBLISHED
3 October 2022

Original content from this work may be used under the terms of the Creative Commons Attribution 4.0 licence.

Any further distribution of this work must maintain attribution to the author(s) and the title of the work, journal citation and DOI.

PAPER

# Fabrication and characterization of a multimodal 3D printed mouse phantom for ionoacoustic quality assurance in image-guided pre-clinical proton radiation research

**Julie Lascaud[1,*], Pratik Dash[1], Katrin Schnürle[1], Jonathan Bortfeldt[1], Katharina Niepel[1], Jessica Maas[2], Matthias Würl[1], Marie Vidal[3], Joël Hérault[3], Guillaume Landry[2,1], Alessandro Stuart Savoia[4], Kirsten Lauber[2,5] and Katia Parodi[1,*]**

[1] Department of Medical Physics, Ludwig-Maximilians-Universität München, Munich, Germany
[2] Department of Radiation Oncology, University Hospital, LMU Munich, Munich, Germany
[3] Centre Antoine Lacassagne—Fédération Claude Lalanne, Nice, France
[4] Department of Industrial, Electronic, and Mechanical Engineering, Roma Tre University, Rome, Italy
[5] German Cancer Consortium (DKTK), partner site Munich, Germany
[*] Authors to whom any correspondence should be addressed.

**E-mail:** j.lascaud@physik.uni-muenchen.de **and** katia.parodi@physik.uni-muenchen.de

**Keywords:** proton therapy, range verification, small animal, phantom, ionoacoustics

Supplementary material for this article is available online

## Abstract

*Objective.* Image guidance and precise irradiation are fundamental to ensure the reliability of small animal oncology studies. Accurate positioning of the animal and the in-beam monitoring of the delivered radio-therapeutic treatment necessitate several imaging modalities. In the particular context of proton therapy with a pulsed beam, information on the delivered dose can be retrieved by monitoring the thermoacoustic waves resulting from the brief and local energy deposition induced by a proton beam (ionoacoustics). The objective of this work was to fabricate a multimodal phantom (x-ray, proton, ultrasound, and ionoacoustics) allowing for sufficient imaging contrast for all the modalities. *Approach.* The phantom anatomical parts were extracted from mouse computed tomography scans and printed using polylactic acid (organs) and a granite/polylactic acid composite (skeleton). The anatomical pieces were encapsulated in silicone rubber to ensure long term stability. The phantom was imaged using x-ray cone-beam computed tomography, proton radiography, ultrasound imaging, and monitoring of a 20 MeV pulsed proton beam using ionoacoustics. *Main results.* The anatomical parts could be visualized in all the imaging modalities validating the phantom capability to be used for multimodal imaging. Ultrasound images were simulated from the x-ray cone-beam computed tomography and co-registered with ultrasound images obtained before the phantom irradiation and low-resolution ultrasound images of the mouse phantom in the irradiation position, co-registered with ionoacoustic measurements. The latter confirmed the irradiation of a tumor surrogate for which the reconstructed range was found to be in reasonable agreement with the expectation. *Significance.* This study reports on a realistic small animal phantom which can be used to investigate ionoacoustic range (or dose) verification together with ultrasound, x-ray, and proton imaging. The co-registration between ionoacoustic reconstructions of the impinging proton beam and x-ray imaging is assessed for the first time in a pre-clinical scenario.

## 1. Introduction

Over the last years, several pre-clinical research platforms have been proposed for precision small animal oncology, mostly in the context of photon therapy for which dedicated commercial systems are already available (Deng *et al* 2007, Clarkson *et al* 2011). To date, there is no counterpart available to support pre-clinical ion or

© 2022 The Author(s). Published on behalf of Institute of Physics and Engineering in Medicine by IOP Publishing Ltd

proton radiation research. In most studies, the animals are irradiated with a clinical ion beam degraded to lower pre-clinical energy. Moreover, only a few groups have included image guidance typically based on x-ray cone beam computed tomography (CBCT) (Ford *et al* 2016, Kim *et al* 2019). Image guidance and precise irradiation of the targeted volume are however fundamental to ensure the reliability of the small animal studies and their scalability to clinical scenarios (Verhaegen *et al* 2018). The phantom fabrication and characterization reported hereafter took place in the context of the development of a novel research platform allowing for precise image-guided irradiation of mice at clinical proton therapy facilities (SIRMIO Parodi *et al* 2019). The irradiation platform will include a dedicated beamline to degrade and focus the incident clinical beam, scaling it down to longitudinal and transverse dimensions more suitable for the irradiation of millimeter size mouse tumors. Ultrasound and proton anatomical imaging in the irradiation position will be employed for daily treatment planning adaptation, and the treatment delivery will be monitored *in vivo* either relying on positron emission tomography in case of continuous beams or based on the so-called ionoacoustics for pulsed beams.

Ionoacoustic range verification takes advantage of the spatially localized dose of proton beams which is favorable to the emission of thermoacoustic waves if the energy is deposited in a short amount of time (ideally in less than about 10 $\mu$s for clinical beams going down to a few hundreds of nanoseconds for pre-clinical mono-energetic beams to ensure stress-confinement (Assmann *et al* 2015, Jones *et al* 2016)). Neglecting heat defects, the energy ($E$) deposited as heat converts to a pressure source (noted $p_0$) proportional to the material-specific Grüneisen parameter ($\Gamma$), which defines the efficiency of the conversion from energy to pressure as indicated in (1), where the deposited energy is expressed in terms of dose ($D$) and medium density ($\rho$) as $E = D \times \rho$

$$p_0 = \Gamma \times D \times \rho. \tag{1}$$

If the volume is heated in a sufficiently short amount of time (stress-confinement), the initial pressure $p_0$ gives rise to a pressure wave-front governed by the thermodynamic wave equation (Hickling *et al* 2018). As it can be seen from (1), measurements of the ionoacoustic signals allow inferring almost direct information on the underlying dose when the energy is deposited in a homogeneous medium and ideally instantaneously (proton pulse duration $\ll$stress-confinement time). Practically, the shape of the signal detected depends on the temporal evolution of the proton pulse and the medium properties (i.e. notably the density and the Grüneisen parameter), such that they all have to be taken into account to reconstruct the proton beam dose in heterogeneous media (Lascaud *et al* 2021, Yu *et al* 2021).

It has been shown over the last decade that the position of the Bragg peak in homogeneous water phantoms can be determined from time-of-flight analysis with accuracy better than one millimeter (Jones *et al* 2015, Lehrack *et al* 2017) and hundred of micrometers (Assmann *et al* 2015) at clinical and pre-clinical energies, respectively. Reconstruction of the initial pressure distribution co-registered with ultrasound (US) anatomical imaging has also been demonstrated experimentally with pre-clinical ion beams (Kellnberger *et al* 2016, Patch *et al* 2016), and more recently the localization of the Bragg peak during the delivery of a clinical treatment plan has been investigated in an anthropomorphic phantom (Patch *et al* 2021). Little work has been done on assessing the accuracy of the initial pressure or dose reconstruction in heterogeneous media. Simulation studies from patient data showed that, with an exact knowledge of the medium properties, the Bragg peak can be reconstructed and located with a millimeter accuracy during breast (van Dongen *et al* 2019), head and liver (Yu *et al* 2019, 2021) irradiation.

However, the quality of ionoacoustics-based dose reconstruction will depend on the accuracy of the medium property estimation. Indeed, information on the density and Grüneisen parameter is required to convert the reconstruction of the initial pressure to a dose distribution. Furthermore, the speed of sound is not constant *in vivo* as it varies depending on the tissue type. The consequences of this are a possible inaccurate estimation of the Bragg peak location derived from the ionoacoustic signal time-of-flight, as well as a potential distortion of the pressure wave-front which needs to be corrected for an accurate reconstruction (Huang *et al* 2012, Cui *et al* 2021). Hence, the complete workflow going from the *in vivo* assessment of the medium properties to the reconstruction of the dose from the ionoacoustic measurements remains to be defined and the accuracy of the resulting registration workflow needs to be evaluated experimentally in a well-known environment.

In this context, we fabricated a mouse phantom aiming for future assessment of the registration workflow and development of methods to evaluate the tissue characteristics (i.e. speed of sound) in an anatomically relevant geometry with known medium properties. Ideally the anthropomorphic phantom should allow to verify the complete irradiation workflow, starting with the contouring of the targeted volume in anatomical imaging (US and proton images), the treatment plan calculation, phantom irradiation, and online verification of the delivery using ionoacoustics in case of pulsed proton beams. Recent progress in 3D printing technologies allows for the fabrication of small animal phantoms with complex and realistic geometry directly extracted from animal computed tomography (CT) scans (Filippou and Tsoumpas 2018), suitable for our application. To the best of our knowledge, whole body 3D printed mouse phantoms proposed to date have focused only on one (e.g. x-ray CT Price *et al* 2020) or two (e.g. x-ray CT and magnetic resonance (Zhang *et al* 2018)) imaging modalities.

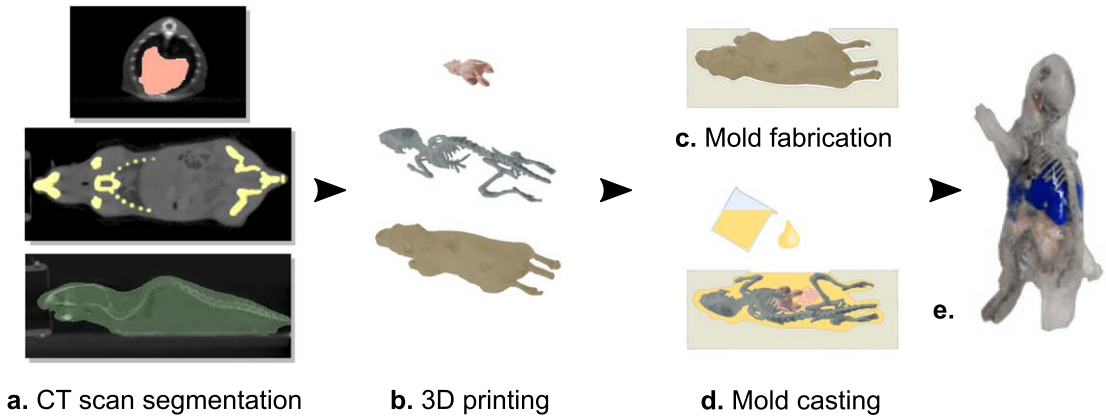


**Figure 1.** Mouse phantom fabrication process: (a) segmentation of the mouse CBCT scans, (b) 3D printing, (c) mold fabrication, and (d) encapsulation of the anatomical parts in the silicone rubber. (e) Picture of the mouse phantom.

The fabrication of a multimodal phantom is however a more challenging task as it requires to use materials able to reproduce tissues on several modalities. Focusing on the imaging modalities that will be available within the SIRMIO system (Parodi *et al* 2019), this includes x-ray and proton imaging (radiography or CT), US imaging, and ionoacoustics, in addition to reasonable proton stopping powers relative to water (close to 1) to realistically reproduce the proton dose deposited in a small animal. Furthermore, as the images (or treatment delivery) maybe done at different locations or repeated over long experimental campaigns, it is important that the anatomy of the phantom remains unchanged, meaning the phantom should be mechanically stable which limited the type of material which can be used (e.g. water-based gels are not suitable). Therefore to facilitate the development, in this work the objective was limited to the fabrication of a phantom with sufficient contrast between the different materials such that several parts of the anatomy could be visualized in all the image modalities. This was achieved by encapsulating 3D printed anatomical pieces extracted from x-ray images of a real mouse in silicone rubber to ensure the mechanical stability of the phantom over time. The properties (stopping power, density, and speed of sound) of the phantom were characterized from bulk materials. Thereafter, images of the mouse phantom were obtained for all the foreseen modalities, including first ionoacoustic experiments with a mono-energetic pre-clinical pulsed proton beam, to validate the phantom interest in supporting the development of image guidance modalities for small animal.

## 2. Material and methods

### 2.1. Mouse phantom preparation

The mouse phantom manufacturing process is summarized in figure 1. The skeleton, organ surrogates, and outer shell were extracted from real mouse CT scans (animal experiments performed according to the FELASA guidelines and upon ethical approval by the Regierung von Oberbayern), as illustrated in figure 1(a). The anatomical parts were 3D printed (figure 1(b)) based on a fused deposition modeling technique using an Ultimaker S3 printer equipped with a 0.6 mm ruby nozzle (3D Solex Everlast HardCore). The mouse's outer part (skin) and organs were printed from standard polylactic acid (PLA, Ultimaker). A filament made of 50 wt.% granite powder mixed with PLA (grey Stonefil, Formfutura) was used for the bone structure. For the latter, the printing parameters were adapted to ensure the extrusion of homogeneous and stable layers (nozzle temperature of 220 °C, layer height of 0.15 mm, with a flow set to 110%). Support structures in polyvinyl alcohol (PVA) were systematically produced to guarantee the good conformity and mechanical stability of the parts during the extrusion. The support was removed at the end of the printing process. The extraction of the skeleton from the support structure is a challenging step because of the small dimensions (e.g. rib with a diameter of about 1 mm) and the brittleness of the PLA/granite mixture. To avoid damaging the printed structure, the skeleton was immersed in warm water (50 °C) for a few seconds to soften the shallow layers of PVA which were gently removed using a brush. The procedure was repeated until most of the PVA was removed, and only a thin layer was kept around the printed skeleton to reinforce it.

Silicone rubber (Elastosil M4601, Wacker Chemie AG) was used to produce tumor surrogates and the intestines. Cylindrical tumors were cut out from 6 mm thick plates of the rubber material using a 2 mm diameter piece cutter. To produce the intestines, thin lines of rubber were deposited onto a polytetrafluoroethylene foil. After 12 h of curing at room temperature, the rubber filaments were rolled up to form the intestines. An

encapsulating mold (figure 1(c)) was produced out of the printed outer shell using modeling paste (Plastilin, Pelikan). The different parts of the mouse phantom were carefully placed in the mold and encapsulated (figure 1(d)) using another silicone rubber (Elastosil 601, Wacker Chemie AG) previously degassed for 5 min at 15 mbar, and cured at room temperature for 24 h.

Additional plates of $18 \times 58 \times 6$ mm$^3$ of the phantom composing materials were manufactured and later used to assess the material properties (i.e. stopping power, density, and speed of sound).

### 2.2. Phantom material characterization

The stopping powers relative to water (SPR) of the phantom materials were estimated using dual-energy computed tomography (DECT). To this aim, the 6 mm thick plates made out of the same materials were scanned using a dual-source scanner (Siemens SOMATOM definition FORCE, Siemens Healthcare, Forchheim Germany) at energies of 90 kVp and 150 kVp with tin filtration (Dedes *et al* 2019). The SPR were calculated following the method proposed by (Saito and Sagara 2017a, 2017b), assuming a ionization potential of 78 eV for water, and a kinetic proton energy of 20 MeV (proton speed relative to the speed of light $\beta = 0.2032$). A dedicated phantom (RMI 467, Gammex, Middleton, USA) was used for the calibration.

The density of the materials ($\rho_{mat}$) was determined based on the Archimedes' principle using a dedicated scale (EMB-V with YDB-02 toolkit, Kern & Sohn GmbH, Germany). The mass of the 6 mm plates were first weighted in air, and subsequently after immersing the sample in water (20 °C, $\rho_{water} = 998.2$ kg m$^{-3}$). The density was evaluated from the mass variation as defined in (2), where $m_{air}$ is the sample mass in air and $m_{water}$ is its mass when immersed in water. The measurement was repeated 10 times for each sample to assess the experimental uncertainties

$$\rho_{mat} = \frac{m_{air}}{m_{air} - m_{water}} \times \rho_{water}. \tag{2}$$

The speed of sound in the different materials was assessed using a through-transmission substitution method (Zeqiri *et al* 2010) in water. Acoustic signals were generated by a 1MHz focused piezoelectric transducer, which has a focal distance of 2 cm, and a 73% fractional bandwidth (V303, Olympus). The transducer was driven by a high-frequency ultrasonic pulser (DPR300 JSR Ultrasonics, Imaginant Inc., USA). After passing through the 6 mm thick plate of the material to be characterized, the ultrasonic wave was acquired at a sampling rate of 156.25 MHz using a 0.5 mm needle hydrophone (Precision Acoustics, United Kingdom) connected to a digital oscilloscope (6404D PicoScope, Pico Technology Ltd., UK). The characterized sample and hydrophone were positioned 2 cm and 4.5 cm distal to the transducer, respectively. The speed of sound in the characterized material ($c_{mat}$) was determined from (3)

$$c_{mat} = \frac{\Delta x \times c_{water}}{\Delta x - \Delta t \times c_{water}}, \tag{3}$$

where $\Delta x$ is the plate thickness, $\Delta t$ is the time difference between a reference signal in water (without material between the transducer and hydrophone) and the signal recorded with the said material, and $c_{water}$ is the speed of sound in water. The time-of-flight was evaluated from the signal envelope and defined as the time corresponding to 10% of the maximum amplitude on the rising edge. The speed of sound in water was determined from the time shift obtained by moving the hydrophone by $\pm 5$ mm along the propagation axis by a step of 1 mm.

### 2.3. Phantom imaging

X-ray CBCT of the phantom was acquired using the small animal radiation research platform (SARRP, X-Strahl, Camberley, UK). The x-ray CBCT was reconstructed from 720 projections (0.5° per image) obtained at an x-ray energy of 60 kV and a current of 0.8 mA (voxel size: $0.26 \times 0.26 \times 0.26$ mm$^3$). Figure 2(a) shows the setup used to capture the US images of the mouse phantom, hereafter referred to as high-resolution ultrasound (HR-US), acquired at 5 MHz with a US linear probe (SP-L01, Interson Corporation, USA). The phantom was immersed in water and only the head and tail regions were laid on holding posts to maintain a water gap of 1 cm below the imaged volume, preventing in this way image reverberation due to the acoustic reflections from the water tank surface. The US probe was mounted onto a three-axis motorized stage and moved along the body length of the mouse with a step of 0.5 mm to obtain multiple two-dimensional images in the transverse plane. The US images were extracted from the JPEG files acquired with the SimpliVue software (Interson Corporation, USA) using an in-house Python routine and concatenated to obtain three-dimensional images. During the image reconstruction, the SimpliVue software assumes a constant speed of sound equal to the average speed of sound in human tissues (i.e. 1540 ms$^{-1}$). For consistency between all the ultrasound imaging modalities, the voxel size along the imaging axis was rescaled to correspond with the speed of sound in the mouse phantom tissue material (grid spacing along the imaging axis $d_z \times v_{tissue}/1540$), leading to a voxel size of $0.06 \times 0.50 \times 0.04$ mm$^3$ along $x$, $y$, and $z$ axes, respectively, as defined in figure 2.

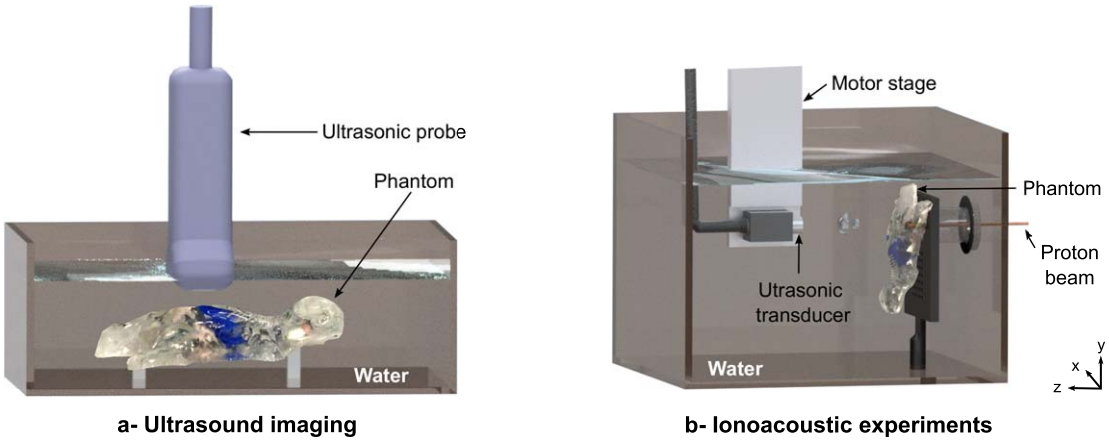


**Figure 2.** Experimental setups used for (a) the ultrasound images, and (b) ionoacoustic measurements co-registered with low-resolution ultrasound.

First feasibility studies in integration mode proton imaging of the phantom were conducted at the ocular treatment beamline belonging to the Medicyc cyclotron at Centre Antoine Lacassagne in Nice (France). Proton radiographies were taken with a large area ($12 \times 14$ cm$^2$ with a pixel size of $0.1 \times 0.1$ mm$^2$) CMOS detector (Teledyne DALSA, Canada) positioned 8 mm downstream to the mouse phantom to acquire coronal projections of the head and abdominal region (Schnürle *et al* 2021). Similar to the method employed by Harms *et al* (2020), the water-equivalent thickness (WET) of the imaged phantom was determined by varying the energy of the incident proton beam. For this purpose, the proton beam was degraded using 0.5 mm thick slabs of polymethylmethacrylate (PMMA). The imaging procedure was repeated for several thicknesses of PMMA up to a total thickness of 27.5 mm, corresponding to 56 energy steps.

### 2.4. Ionoacoustic experiments

Ionoacoustics experiments were carried out at the tandem accelerator of the Maier-Leibnitz Laboratory in Munich (Germany) with a 20 MeV pulsed proton beam (200 ns square pulse, beam current of 3.5 nA at a repetition rate of 10 kHz). Figure 2(b) shows the setup used to investigate the ionoacoustic emission and its propagation in the mouse phantom. The phantom was immersed in a water tank closed by a 50 $\mu$m thick polyimide foil after a 6 cm air channel. The phantom was positioned such that the proton beam was irradiating the tumor surrogate implanted in the left hind leg, with the phantom flank side touching the polyimide foil. The acoustic signals were acquired using a 12 MHz capacitive micromachined ultrasonic transducer (CMUT) with a bias voltage set to 75% of the collapse voltage ($V_{collapse} = 310$ V). The signals were amplified by a low-noise voltage amplifier (HVA-10M-60-B, FEMTO Messtechnik GmbH, Germany) with a gain of 60 dB and acquired using a digital oscilloscope (6404D PicoScope, Pico Technology Ltd., UK) at a sampling frequency of 156.25 MHz. The CMUT detector was mounted on a three-axis motorized stage and positioned on the proton beam axis. During the experiments, the ultrasonic transducer was moved laterally in the transverse plane along the $x$-axis (see figure 2(b)) by step of 0.5 mm over a distance of $\pm 10$ mm from the proton beam axis. For each position, the measurements were repeated over 1000 pulses (acquisitions) and averaged to improve the signal-to-noise ratio.

Ultrasound pulse-echoes measurements were performed consecutively to the ionoacoustic experiments to obtain a low-resolution image (LR-US) of the phantom anatomy in the same plane. To this end, the transducer was moved by $\pm 10$ mm and the step was reduced to 0.25 mm to improve the lateral resolution of the image. The CMUT was connected to the high-frequency ultrasonic pulser operating in pulse-echo mode. A 70 ns negative pulse of 5 V was used in transmission, whereas the signal was amplified by 30 dB and low-pass filtered ($f_{cutoff} = 20.5$ MHz) in reception.

### 2.5. Image registration

A similar reconstruction was performed for both the ionoacoustic and low-resolution ultrasound images. The average signals were filtered using fourth-order band-pass Butterworth filters (between 0.5 MHz and 8 MHz and 2 MHz–15 MHz for the ionoacoustic and ultrasound measurements, respectively). The signal envelope was calculated from the absolute value of the Hilbert transform and a homogeneous medium, with the speed of sound equal to the speed of sound in the tissue-mimicking material, was assumed. Accurate temporal co-registration of the two data sets (i.e. ionoacoustics and ultrasound) requires starting the acquisition of the

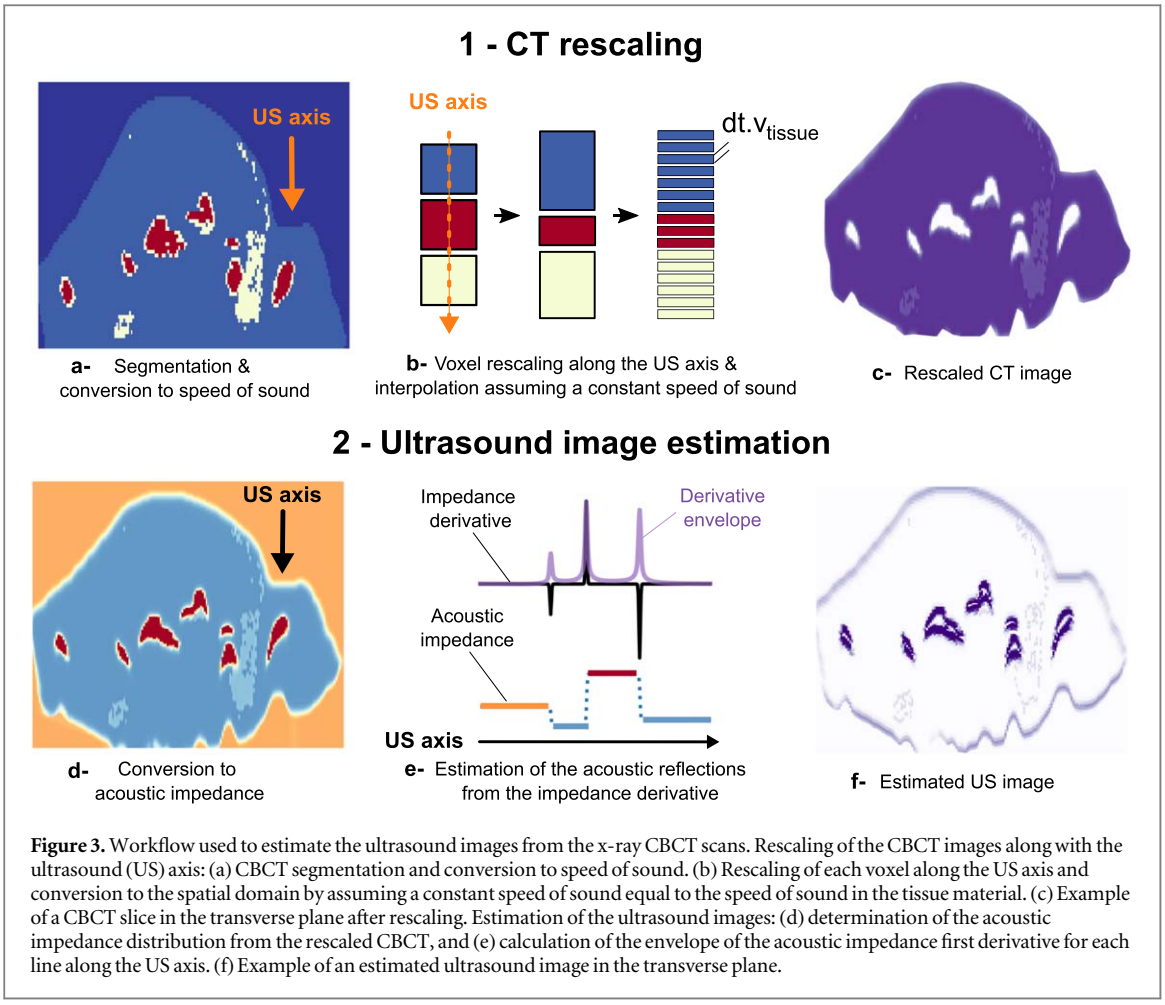


**Figure 3.** Workflow used to estimate the ultrasound images from the x-ray CBCT scans. Rescaling of the CBCT images along with the ultrasound (US) axis: (a) CBCT segmentation and conversion to speed of sound. (b) Rescaling of each voxel along the US axis and conversion to the spatial domain by assuming a constant speed of sound equal to the speed of sound in the tissue material. (c) Example of a CBCT slice in the transverse plane after rescaling. Estimation of the ultrasound images: (d) determination of the acoustic impedance distribution from the rescaled CBCT, and (e) calculation of the envelope of the acoustic impedance first derivative for each line along the US axis. (f) Example of an estimated ultrasound image in the transverse plane.

ionoacoustic signals at the exact time when the proton beam enters the phantom. In our experiments, the signal acquisition was triggered by the synchronization signal provided by the chopper system of the tandem accelerator which is generated before the proton burst reaches the experimental site. To compensate for that, an offset of $-1.43$ $\mu$s was systematically applied to the ionoacoustic measurements as determined in a previous study (Wieser *et al* 2020). It is worth noting that the spatial registration of the two modalities was ensured by using the same transducer.

In heterogeneous media, ultrasound images usually suffer from distortions due to the assumption of a constant speed of sound in the reconstruction (speed of sound aberration Fontanarosa *et al* 2011). To facilitate the registration, US images were evaluated from the x-ray CBCT scans as summarized in figure 3. The CBCT images were first rescaled along the US axis (figure 3(c)). To this aim, scans in the region of interest were segmented into four different materials: air, tissue surrogate, bone surrogate, and tumor mimicking material and converted to a speed of sound, as illustrated in figure 3(a). The speeds of sound were defined based on the previous characterizations, whereas the air was substituted by water ($c_{water} = 1484$ m s$^{-1}$). Each voxel was rescaled along the US axis by converting it to the time it takes for the US waves to propagate through the voxel dimension, and converted back to the spatial domain by assuming a constant speed of sound equal to the speed of sound in the tissue material (see figure 3(b)). Finally, the US images were estimated from the rescaled CBCT scans, as depicted in figure 3(f). The scans were converted to an acoustic impedance image (figure 3(d)) and the envelope of the acoustic impedance first derivative was calculated for each line along the US axis (figure 3(e)).

## 3. Results

### 3.1. Material properties

The properties of the phantom materials are summarized in table 1. The material SPR varies from 1.023 for the tissue substitute to 1.501 for the bone-mimicking material, which is comparable to SPR values in tissues (typically ranging from 0.95 for adipose tissues up to 1.6 for bones Schaffner and Pedroni 1998). The speed of sound for the tissue- and tumor mimicking materials was found to be around 1047 m s$^{-1}$ and 1022 m s$^{-1}$, respectively, which is in good agreement with the values previously reported (Zell *et al* 2007). The speed of sound

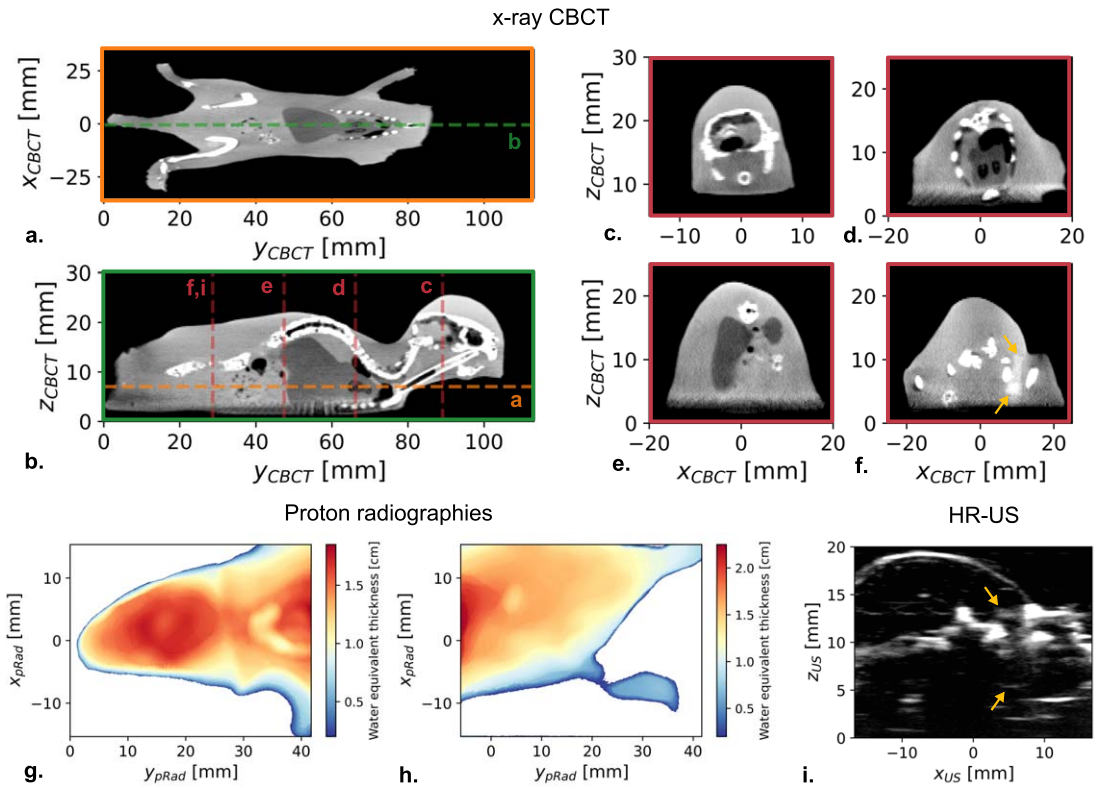


**Figure 4.** Mouse phantom imaging. X-ray CBCT in (a) a coronal plane, (b) a sagittal plane, and transverse planes of (c) the head, (d) the chest cavity, (e) the abdominal region (liver and right kidney), and (f) the hind legs, including the implanted tumor surrogate. The dashed line indicates the position of the different slices. Proton radiographies of the mouse phantom corresponding to the (g) head and (h) abdominal region in the coronal plane. (i) Transverse high-resolution ultrasound image (HR-US) of the left hind leg. The yellow arrows indicate the position of the tumor surrogate.

**Table 1.** Properties of the phantom materials.

| Material | SPR[a] | Density[b] (kg m$^{-3}$) | Speed of sound[c] ( m s$^{-1}$) |
|---|---|---|---|
| Elastosil 601 (tissue) | 1.023 ± 0.008 | 1019 ± 4 | 1047 ± 1 |
| Elastosil M4601 (tumor) | 1.139 ± 0.008 | 1132 ± 6 | 1022 ± 1 |
| PLA (organs) | 1.174 ± 0.011 | 1237 ± 4 | 2324 ± 5 |
| PLA + granite (bones) | 1.501 ± 0.014 | 1552 ± 7 | 1829 ± 8[d] |

Mean and standard deviation observed for:

[a] Voxels contained in a volume of 7.5 × 4 × 40 mm$^3$ at the center of the 6 mm plates (total of 15 000 voxels).

[b] 10 measurements.

[c] 10 measurements.

[d] Detection threshold increased from 10% to 50% of the maximum amplitude due to the low signal-to-noise ratio of the measurements.

in the rubbers is 30% lower than the speed of sound in tissue (typically 1540 ms$^{-1}$). However, the resulting acoustic impedance amounts to 1.07 MRayls and 1.17 MRayls for the tissue and tumor surrogates, respectively, which provides realistic acoustic contrast between the two types of tissues material (Culjat *et al* 2010). The characteristics of the substitute bone material are consistent with the properties of real bones, whereas both the density and speed of sound in the printed PLA are higher than what is typically observed for soft tissues.

### 3.2. Validation of the imaging capability

The images of the mouse phantom obtained from the different modalities are presented in figure 4. Coronal and sagittal views extracted from the x-ray CBCT are depicted in figures 4(a), (b), and transverse images are presented in figures 4(c)–(f). The x-ray CBCT scans reveal the fine structure of the bone substitute i.e. skull and ribs in figures 4(a)–(d), and spine in figures 4(b)–(e). PVA residues can be observed in the intercostal regions, as well as air pockets in the chest cavity that were trapped during the manufacturing process. The air cavity at $y = 65$ mm (figures 4(a), (b)) corresponds to the printed heart which is attached to the liver surrogate, and the air pockets observed between $y = 35$ mm and $y = 45$ mm is the intestine region.

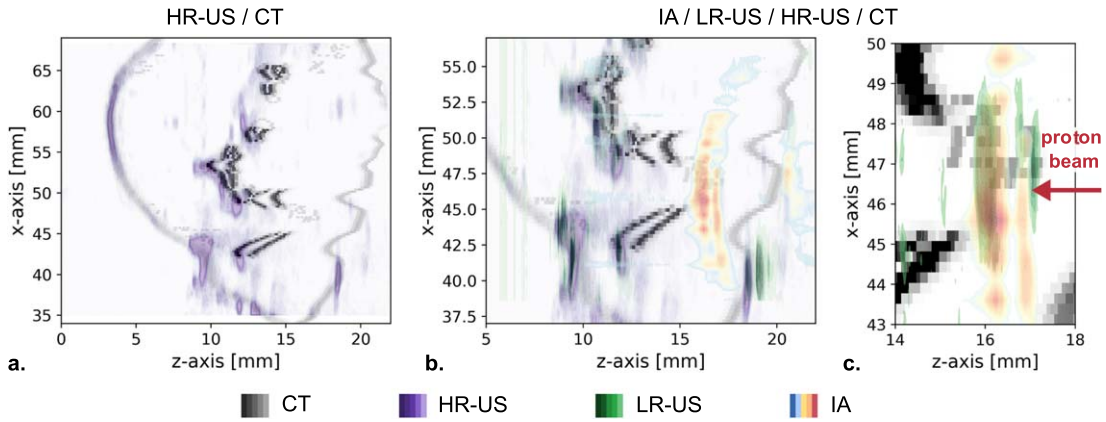


**Figure 5.** Ionoacoustic experiments and co-registration with ultrasound. (a) Estimated ultrasound images (grey) obtained from the x-ray CT overlaid to the high-resolution ultrasound image (HR-US, in purple). HR-US and CT superimposed to the low-resolution ultrasound (LR-US, in green) co-registered to the envelope of the ionoacoustic signals measured at different lateral positions (IA, blue to red color scale): (b) large view, and (c) zoom in the targeted area (tumor surrogate). The contrast in the LR-US in (c) was increased for better visualization of the tumor boundaries. The IA corresponds to isocontours of the signal envelopes with amplitude superior to 50% of the maximum amplitude. The red arrow shows the direction of the proton beam relative to the phantom anatomy.

The proton radiographies of the mouse phantom head and abdominal region are presented in figures 4(g), (h), respectively. The water equivalent thickness of the head region goes up to 1.85 cm on the top of the skull and the smaller imaged thicknesses at around $y = 35$ mm corresponds to the air pockets trapped in the chest cavity. The lower part of the left kidney is observed in figure 4(h) (water equivalent thickness of up to 2.25 cm), in good agreement with the expectations (see figure S1 of the supporting material available online at stacks.iop.org/PMB/67/205001/mmedia). It should be noted that the visible contours blurring are due to multiple Coulomb scattering of the protons in the phantom and further scattering in the air gap between the imaged object and detector (Würl *et al* 2020). Figure 4(i) shows the HR-US around the left hind leg (same transverse plane as figure 4(f)), mostly depicting the skin of the mouse phantom and bone structures. The two sides of the cylindrical tumor surrogate are visible in the US image (marked by the yellow arrows on figure 4(i)), confirming a sufficient acoustic contrast between the tissue and tumor surrogate materials.

### 3.3. Ionoacoustic monitoring of a pre-clinical proton beam

The results of the registration experiments are shown in figure 5. Figure 5(a) depicts the registration of the US image estimated from the x-ray CBCT scans (CT) and the HR-US image obtained with the linear array (figure 4(i)). There is a good agreement between the two images, in particular on the outer contour of the mouse phantom (skin). The discrepancies observed in the image of the internal structures are attributed to different lateral resolutions of the two imaging modalities (0.26 mm for the x-ray CBCT image and 2 mm for the HR-US estimated from previous measurements with a wire phantom).

The registration between all the imaging modalities is presented in figures 5(b), (c). The images acquired during the in-beam experiments (LR-US and IA) were overlaid in figures 5(b), (c) by aligning the LR-US and HR-US images. The ionoacoustic signal is composed of two main components. The first (at around 16 mm on the $z$-axis) is the direct acoustic signal generated in the Bragg peak region mostly due to the sharp energy gradient distal to the Bragg peak. The second part is observed at 20 mm $z$-axis position and corresponds with the position where the proton beam enters the mouse phantom (phantom skin). This ionoacoustic entrance signal is caused by the gradient of energy and Grüneisen parameter variation at the interface between the mouse phantom and the surrounding water. Taking a closer look around the tumor region (figure 5(c)), it can be seen that the direct signal is split into two pulses. A part of the signal matches with the acoustic reflection at the interface between the tumor and tissue materials visualized on the LR-US. Similar to the entrance signal, this second pulse of the direct signal corresponds to the acoustic wave generated due to the variation of the Grüneisen parameter and of the deposited energy between the two materials (density and Grüneisen parameter of the tumor surrogate expected to be larger than the tissue mimicking material, see supporting material). The imaged distance between the maximum amplitude of the direct ionoacoustic signal and the mouse phantom entrance in the LR-US on the same line is about 3.8 mm. Considering the SPR of the silicone rubber materials (superior to 1, see table 1), the estimated range is in reasonable agreement with the expected value (range in water at 90% equal to 4.17 mm). It should be noted that, although this was not quantified, it is reasonable to assume that the proton beam penetrated a thin layer of water before entering the phantom since the experiments were performed in water.

## 4. Discussion

### 4.1. Future phantom development

In this study, we showed that using commercially available PLA and PLA/granite filaments, the organs and bone structure of a mouse can be accurately reproduced and imaged using several modalities including x-ray CBCT, proton radiography, and US, offering a realistic tool to investigate multimodal imaging. The stopping power of the proposed phantom materials evaluated from dual-energy CT agrees with corresponding tissues' values, making the phantom suitable for use in quality assurance in proton therapy. To this end, the insertion of a dosimetric tool will allow to verify the conformity of the delivered dose by comparison with the treatment plan (Soultanidis *et al* 2019).

Both PLA and the silicone rubbers used as soft tissue surrogates ensure the mechanical stability of the phantom while preventing any change of phantom anatomy which would hamper its adoption for quality assurance. However, the speed of sound in these materials differs from those in soft tissues and these materials do not optimally reproduce the acoustic wave scattering and attenuation. The former limitation requires applying a correction to the US images to compensate for the speed of sound of 1540 m $s^{-1}$ assumed by most commercially available US systems. The latter may lead to erroneous conclusions on the investigated multimodal co-registration workflow and potential segmentation of the US image (e.g. to delineate the tumor contour) if not corrected. US phantoms typically rely on materials with high water content such as agarose, gelatin or polyvinyl alcohol gel (Culjat *et al* 2010). However, such materials require specific storage to prevent them from drying out, cannot be kept for a long time, and can easily be deformed. Furthermore, the fabrication of these tissue surrogates is mostly based on casting methods which constrain the shape and dimension of the parts to only have a relatively simple geometry and a size of the order of millimeters.

Stereolithography printing (SLA) of silicone-based resins loaded with higher speed of sound materials (In *et al* 2017) or small scale variation of the curing parameters for each printed layer (Paulsen *et al* 2021) could be a more promising alternative. It is interesting to note that commercially available SLA printers offer printing resolution usually better than 50 $\mu$m (e.g. 25 $\mu$m resolution for the Form 3+, Formlabs). In addition to the high fidelity of the printings obtained from SLA printers, the high resolution offered could also enable the manufacturing of organs with embedded vascular structures (Ommen *et al* 2021) which makes them ideal for the investigation of contrast agents.

### 4.2. Imaging and registration workflow

The proposed mouse phantom, eventually associated to implanted dosimetric tools, will support the development of small animal proton irradiator (SIRMIO). Within the SIRMIO platform, the treatment plan will be derived from US images of the tumor volume (either obtained during the mouse preparation or after positioning the animal on the irradiation platform) registered to proton tomography of the mouse in the treatment position, providing accurate estimation of the tissue stopping power. Proton radiography may also be employed for alignment or registered to pre-treatment x-ray CBCT scans to reduce the imaging time after positioning the mouse on the SIRMIO platform (Palaniappan *et al* 2022). For pulsed proton beams (i.e. at clinical facilities equipped a synchro-cyclotron accelerator), the treatment delivery will be monitored using ionoacoustics, ideally in quasi-real-time, to interrupt the irradiation in case of large deviations between the planned and actually delivered dose or adapt the treatment plan from one fraction to the other.

Accurate reconstruction of the proton dose from ionoacoustic measurements at multiple locations in a small animal requires a correct estimation of the tissue properties. In this work, the x-ray CBCT scans were used to derive an estimation of the US images by knowing the medium properties (i.e. density and speed of sound) from the previous characterizations of the different materials. The estimated US images were thereafter aligned to US pulse-echo measurements of the phantom in the irradiation position, allowing for a visualization of the ionoacoustic signals relative to the phantom anatomy imaged with the CBCT. The proposed registration workflow was utilized as a first proof-of-principle of the phantom interest in such a co-registration study and feasibility of ionoacoustics-based range verification method but needs to be further investigated in real applications where the speed of sound is unknown. In that case, a first estimation of the medium properties could be derived from the x-ray CT scans (conversion of the Hounsfield units to density and speed of sound Mast 2000) or directly imaged with ultrasound using a dedicated reconstruction method (Sak *et al* 2017, Rau *et al* 2021). More extensive work is also required to estimate the Grüneisen parameter *in vivo* which will play a fundamental role in the conversion from pressure to absolute dose.

Although the present results are a first demonstration of co-registration between x-ray CBCT, US, and ionoacoustics images, it is not possible to conclude on the accuracy of the ionoacoustics-based range verification method. This is due to the uncertainties on the mouse phantom positioning during the experiments, and in particular on the thickness of the possible small water gap between the phantom flat side and the entrance

window of the water tank used. In real applications with mice, the acoustic coupling required for the detection of the ionoacoustic signals generated during the treatment delivery cannot be done by immersing the animal in water as the additional water layer will make more complex the treatment plan calculation and will reduce the quality of the proton imaging (i.e. required an increase of the energy of the proton beam used for imaging which will results in a larger energy spread and hence a decrease of the energy and imaging resolution). Therefore, the acoustic detectors are foreseen to be placed directly onto the mouse skin, and optimally positioned to not interfere with the treatment delivery and pre-treatment proton imaging (Lascaud *et al* 2021). Considering the space limitation, only a few spare sensors are expected to be used for both ionoacoustic and low-resolution ultrasound images. Similarly to the workflow presented hereby, the low-resolution ultrasound images will be used to facilitate the registration between the ionoacoustic reconstructions and the other (high-resolution) anatomical images.

Hereby, we demonstrated that proton radiography in integration mode which enables imaging with a high instantaneous particle flux delivered by a pulsed proton beam allows to appreciate the morphology of the small animal. Further studies should investigate the registration between the US and proton imaging for which the different image contrast compared to x-ray images, the possibly lower spatial resolution due to proton scattering in the imaged object, and an inaccurate conversion from SPR to Hounsfield units may affect the accuracy of the speed of sound and Grüneisen parameter evaluation. Moreover, the integration of the anatomical information obtained from ultrasound and the relative location of the Bragg peak estimated from the ionoacoustic measurements in a (pre-)clinical workflow needs to be assessed. In particular, here the reconstructed initial pressure was overlaid with the US images and deformed CBCT but an additional correction of the speed of sound aberration in the US images will be required to provide accurate information on the anatomy relevant for the treatment planning.

### 4.3. Ionoacoustic range verification in small animal with clinical proton beams

The present study was carried out with an ideal quasi-monoenergertic 20 MeV proton beam with proton pulses of 200 ns, which leads to strong ionoacoustic emissions in the MHz range with amplitudes up to 100 Pa facilitating the signal detection. The degradation of a clinical proton beam is expected to results in a larger energy spread and consequently an increase of the longitudinal dimension of the Bragg peak volume (Gerlach *et al* 2020). Assuming measurements at a clinical synchro-cyclotron facility which is the only type of clinical proton accelerator able to deliver a pulsed beam without requiring modification of the accelerator control system, the proton pulse is a few $\mu$s Gaussian pulse (Lehrack *et al* 2017). In these conditions, much lower ionoacoustic frequency and amplitudes are expected than the present study. The final characteristics of the acoustic waves will mostly depend on the performances of the SIRMIO beamline which remains to be clarified. However, it is anticipated that both pressure level and frequency will be in the same order of magnitude (or even lower) than clinical ionoacoustic applications (presumably in the mPa range and below 100 kHz, see figure S3 of the supporting material). Consequently, the first challenge to be overcome in the use of ionoacoustic at clinical facilities will be the detection of the acoustic signals. The accuracy and precision of the range verification methods in these conditions remain to be evaluated.

## 5. Conclusion

In this study, we fabricated and characterized a multimodal 3D printed small animal phantom. The phantom anatomical parts were extracted from mouse computed tomography scans and printed using polylactic acid (organs) and polylactic acid mixed with granite powder (skeleton). The anatomical pieces were encapsulated in silicone rubber to ensure long-term stability. The phantom was imaged using x-ray cone-beam computed tomography, proton radiography, ultrasound imaging, and pulsed proton beam monitoring using ionoacoustics. The different anatomical parts could be visualized in all the imaging modalities and reasonable range estimates were deduced from the proposed workflow, thus validating the phantom use for multimodal imaging to support the development of a small animal proton irradiator.

## Acknowledgments

This work was funded by the European Research Council (SIRMIO, Grant No. 725 539). The authors acknowledge the financial support from the German Research Foundation (Excellence Cluster 'Munich Center for Advanced Photonics'), the Centre for Advanced Laser Applications, and the BFHZ (BayFrance grant FK312019). The authors would like to thank: Prof. Bastian Sabel for organizing the DECT scans; Romy Knab for her support in the phantom fabrication; Grigory Liubchenko for his help in the acquisition and reconstruction of the x-ray CBCT scans; Dr. Petter Hofverberg for his support during the proton image acquisition; Barbara

Mauti for her support in the packaging of the CMUT probe used in the experiments; Prof. Günther Dollinger and Jannis Schauer for providing the function generator used to control the chopper system of the tandem accelerator; PD Dr. Walter Assmann, Dr. Hans-Peter Wieser, Ronaldo Kalunga, and Benjamin Wollant for their help in the preparation of the first experiments.

## Data availability statement

The data supporting the findings of this study are openly available online at: https://doi.org/10.5281/ zenodo.6988993

## ORCID iDs

Julie Lascaud https://orcid.org/0000-0002-7649-6909
Pratik Dash https://orcid.org/0000-0001-9180-2065
Matthias Würl https://orcid.org/0000-0003-3044-449X
Guillaume Landry https://orcid.org/0000-0003-1707-4068
Katia Parodi https://orcid.org/0000-0001-7779-6690

## References

Assmann W *et al* 2015 Ionoacoustic characterization of the proton bragg peak with submillimeter accuracy *Med. Phys.* **42** 567–74
Clarkson R, Lindsay P, Ansell S, Wilson G, Jelveh S, Hill R and Jaffray D 2011 Characterization of image quality and image-guidance performance of a preclinical microirradiator *Med. Phys.* **38** 845–56
Cui M, Zuo H, Wang X, Deng K, Luo J and Ma C 2021 Adaptive photoacoustic computed tomography *Photoacoustics* **21** 100223
Culjat M O, Goldenberg D, Tewari P and Singh R S 2010 A review of tissue substitutes for ultrasound imaging *Ultrasound Med. Biol.* **36** 861–73
Dedes G *et al* 2019 Experimental comparison of proton ct and dual energy x-ray ct for relative stopping power estimation in proton therapy *Phys. Med. Biol.* **64** 165002
Deng H, Kennedy C W, Armour E, Tryggestad E, Ford E, McNutt T, Jiang L and Wong J 2007 The small-animal radiation research platform (sarrp): dosimetry of a focused lens system *Phys. Med. Biol.* **52** 2729-2740
Filippou V and Tsoumpas C 2018 Recent advances on the development of phantoms using 3d printing for imaging with ct, mri, pet, spect, and ultrasound *Med. Phys.* **45** e740–60
Fontanarosa D, Van Der Meer S, Harris E and Verhaegen F 2011 A ct based correction method for speed of sound aberration for ultrasound based image guided radiotherapy *Med. Phys.* **38** 2665–73
Ford E *et al* 2016 An image-guided precision proton radiation platform for preclinical *in vivo* research *Phys. Med. Biol.* **62** 43-58
Gerlach S *et al* 2020 Beam characterization and feasibility study for a small animal irradiation platform at clinical proton therapy facilities *Phys. Med. Biol.* **65** 245045
Harms J M, Maloney L, Sohn J J, Erickson A, Lin Y and Zhang R 2020 Flat-panel imager energy-dependent proton radiography for a proton pencil-beam scanning system *Phys. Med. Biol.* **65** 145001
Hickling S, Xiang L, Jones K C, Parodi K, Assmann W, Avery S, Hobson M and El Naqa I 2018 Ionizing radiation-induced acoustics for radiotherapy and diagnostic radiology applications *Med. Phys.* **45** e707–21
Huang C, Nie L, Schoonover R W, Guo Z, Schirra C O, Anastasio M A and Wang L V 2012 Aberration correction for transcranial photoacoustic tomography of primates employing adjunct image data *J. Biomed. Opt.* **17** 066016
In E, Walker E and Naguib H 2017 Novel development of 3d printable uv-curable silicone for multimodal imaging phantom *Bioprinting* **7** 19–26
Jones K C, Seghal C M and Avery S 2016 How proton pulse characteristics influence protoacoustic determination of proton-beam range: simulation studies *Phys. Med. Biol.* **61** 2213–42
Jones K C, Vander Stappen F, Bawiec C R, Janssens G, Lewin P A, Prieels D, Solberg T D, Sehgal C M and Avery S 2015 Experimental observation of acoustic emissions generated by a pulsed proton beam from a hospital-based clinical cyclotron *Med. Phys.* **42** 7090–7
Kellnberger S, Assmann W, Lehrack S, Reinhardt S, Thirolf P, Queirós D, Sergiadis G, Dollinger G, Parodi K and Ntziachristos V 2016 Ionoacoustic tomography of the proton bragg peak in combination with ultrasound and optoacoustic imaging *Sci. Rep.* **6** 1–7
Kim M M, Irmen P, Shoniyozov K, Verginadis I I, Cengel K A, Koumenis C, Metz J M, Dong L and Diffenderfer E S 2019 Design and commissioning of an image-guided small animal radiation platform and quality assurance protocol for integrated proton and x-ray radiobiology research *Phys. Med. Biol.* **64** 135013
Lascaud J, Dash P, Wieser H-P, Kalunga R, Würl M, Assmann W and Parodi K 2021 Investigating the accuracy of co-registered ionoacoustic and ultrasound images in pulsed proton beams *Phys. Med. Biol.* **66** 185007
Lascaud J *et al* 2021 Optimization of the backing material of a low frequency pvdf detector for ion beam monitoring during small animal proton irradiation *2021 IEEE Int. Ultrasonics Symp. (IUS), IEEE* pp 1–4
Lehrack S *et al* 2017 Submillimeter ionoacoustic range determination for protons in water at a clinical synchrocyclotron *Phys. Med. Biol.* **62** L20-L30
Mast T D 2000 Empirical relationships between acoustic parameters in human soft tissues *Acoust. Res. Lett. Online* **1** 37–42
Ommen M L, Schou M, Beers C, Jensen J A, Larsen N B and Thomsen E V 2021 3d printed calibration micro-phantoms for super-resolution ultrasound imaging validation *Ultrasonics* **114** 106353
Palaniappan P, Meyer S, Rädler M, Kamp F, Belka C, Riboldi M, Parodi K and Gianoli C 2022 X-ray ct adaptation based on a 2d-3d deformable image registration framework using simulated in-room proton radiographies *Phys. Med. Biol.* **67** 045003
Parodi K *et al* 2019 Towards a novel small animal proton irradiation platform: the sirmio project *Acta Oncol.* **58** 1470–5

Patch S K *et al* 2021 Thermoacoustic range verification during pencil beam delivery of a clinical plan to an abdominal imaging phantom *Radiother. Oncol.* **159** 224–30

Patch S *et al* 2016 Thermoacoustic range verification using a clinical ultrasound array provides perfectly co-registered overlay of the bragg peak onto an ultrasound image *Phys. Med. Biol.* **61** 5621–38

Paulsen S J *et al* 2021 Projection-based stereolithography for direct 3d printing of heterogeneous ultrasound phantoms *PLoS One* **16** e0260737

Price G *et al* 2020 An open source heterogeneous 3d printed mouse phantom utilising a novel bone representative thermoplastic *Phys. Med. Biol.* **65** 10NT02

Rau R, Schweizer D, Vishnevskiy V and Goksel O 2021 Speed-of-sound imaging using diverging waves *Int. J. Comput. Assisted Radiol. Surgery* **16** 1201–11

Saito M and Sagara S 2017a A simple formulation for deriving effective atomic numbers via electron density calibration from dual-energy ct data in the human body *Med. Phys.* **44** 2293–303

Saito M and Sagara S 2017b Simplified derivation of stopping power ratio in the human body from dual-energy ct data *Med. Phys.* **44** 4179–87

Sak M, Duric N, Littrup P, Bey-Knight L, Ali H, Vallieres P, Sherman M E and Gierach G L 2017 Using speed of sound imaging to characterize breast density *Ultrasound Med. Biol.* **43** 91–103

Schaffner B and Pedroni E 1998 The precision of proton range calculations in proton radiotherapy treatment planning: experimental verification of the relation between ct-hu and proton stopping power *Phys. Med. Biol.* **43** 1579–92

Schnürle K *et al* 2021 Development of integration mode proton imaging with a single cmos detector for a small animal irradiation platform *Phys. Med.* **92** S41–2

Soultanidis G *et al* 2019 Development of an anatomically correct mouse phantom for dosimetry measurement in small animal radiotherapy research *Phys. Med. Biol.* **64** 12NT02

van Dongen K, de Blécourt A, Lens E, Schaart D and Vos F 2019 Reconstructing 3d proton dose distribution using ionoacoustics *Phys. Med. Biol.* **64** 225005

Verhaegen F *et al* 2018 Estro acrop: technology for precision small animal radiotherapy research: optimal use and challenges *Radiother. Oncol.* **126** 471–8

Wieser H-P, Huang Y, Schauer J, Lascaud J, Chmyrov A, Ntziachristos V, Dollinger G, Assmann W and Parodi K 2020 Experimental demonstration of accurate bragg peak localization with ionoacoustic tandem phase detection (itpd) *Physics in Medicine& Biology* **66** 255020

Würl M, Gianoli C, Englbrecht F S, Schreiber J and Parodi K 2020 A monte carlo feasibility study on quantitative laser-driven proton radiography *Z. Med. Phys.* **32** 109–19

Yu Y, Li Z, Zhang D, Xing L and Peng H 2019 Simulation studies of time reversal-based protoacoustic reconstruction for range and dose verification in proton therapy *Med. Phys.* **46** 3649–62

Yu Y, Qi P and Peng H 2021 Feasibility study of 3d time-reversal reconstruction of proton-induced acoustic signals for dose verification in the head and the liver: a simulation study *Med. Phys.* **48** 4485–97

Zell K, Sperl J I, Vogel M W, Niessner R and Haisch C 2007 Acoustical properties of selected tissue phantom materials for ultrasound imaging *Phys. Med. Biol.* **52** N475-N484

Zeqiri B, Scholl W and Robinson S P 2010 Measurement and testing of the acoustic properties of materials: a review *Metrologia* **47** S156–71

Zhang H, Hou K, Chen J, Dyer B A, Chen J-C, Liu X, Zhang F, Rong Y and Qiu J 2018 Fabrication of an anthropomorphic heterogeneous mouse phantom for multimodality medical imaging *Phys. Med. Biol.* **63** 195011